MATERIALS SCIENCE

A multiaxial lead-free two-dimensional organic-inorganic perovskite ferroelectric

Chao-Ran Huang[1], Xuzhong Luo[1,*], Xiao-Gang Chen[2], Xian-Jiang Song[2], Zhi-Xu Zhang[2] and Ren-Gen Xiong [ID][2,*]

ABSTRACT

Two-dimensional (2D) hybrid organic-inorganic perovskites (HOIPs) have recently gained tremendous interest because of their unique features in contrast to three-dimensional counterparts and traditional 2D materials. However, although some 2D HOIP ferroelectrics have been achieved, the issue of toxic Pb and uniaxial nature impede their further application. Herein, for the first time, we report a lead-free 2D HOIP multiaxial ferroelectric, $[3,3$-difluorocyclobutylammonium$]_2CuCl_4$ (**1**), which shows four ferroelectric axes and eight equivalent polarization directions, more than those of the other 2D HOIP ferroelectrics and even the inorganic perovskite ferroelectric $BaTiO_3$ (three ferroelectric axes and six equivalent polarization directions). **1** also features a high Curie temperature of 380 K and exhibits remarkable thermochromism of color change from green-yellow to dark brown. To our knowledge, **1** is the first multiaxial lead-free 2D HOIP ferroelectric. This work sheds light on the exploration of better lead-free 2D HOIP ferroelectrics.

Keywords: ferroelectrics, organic-inorganic perovskites, multiaxial ferroelectrics, Curie temperature, thermochromism

[1]Key Laboratory of Organo-Pharmaceutical Chemistry of Jiangxi Province, College of Chemistry and Chemical Engineering, Gannan Normal University, Ganzhou 341000, China and [2]Jiangsu Key Laboratory for Science and Applications of Molecular Ferroelectrics, Southeast University, Nanjing 211189, China

*Corresponding authors. E-mails: luoxz@gnnu.edu.cn; xiongrg@seu.edu.cn

INTRODUCTION

Perovskite-type materials have received remarkable attention all over the world since they were discovered and investigated [1–3]. The large family of perovskites are acting as potential candidates for electronic and photoelectronic devices [4–6]. In recent years, the rapid development of three-dimensional (3D) $CH_3NH_3PbI_3$-based perovskite solar cells has aroused great research interest in the area of low-cost and easily solution-processable hybrid organic-inorganic perovskites (HOIPs) [7–10]. Among them, the two-dimensional (2D) lead halide HOIPs, which have good moisture resistance, compositional diversity, quantum-well electronic structure, broadband emission and layer-tunable photoelectronic properties in contrast to 3D counterparts, are attracting increasing attention [11–14]. These features and the rich physical properties also make 2D HOIPs unique from conventional 2D materials including graphene, graphdiyne, MoS_2 and WS_2 [15,16]. 2D HOIPs adopt the typical crystal structure of organic cationic layer alternating with the 2D inorganic anionic framework [11–14]. This structural feature provides a great opportunity for arousing the ferroelectricity [17,18], which shows a crucial role in ferroelectric random access memory, piezoelectric devices and capacitors [19–23]. Ferroelectricity was found in a number of lead halide 2D HOIPs [24–35], such as (4,4-diflorocyclohexylammonium)$_2$PbI$_4$ [24], $(C_5H_{10}CHNH_3)_2PbBr_4$ [25], $(C_6H_5CH_2NH_3)_2PbCl_4$ [26], $[CH_3(CH_2)_3NH_3]_2(CH_3NH_3)Pb_2Br_7$ [27] and $(C_4H_9NH_3)_2(NH_2CHNH_2)Pb_2Br_7$ [28]. Some of them show excellent ferroelectric performance of high Curie temperature and large piezoelectric voltage coefficient [33,34]. However, the environmental toxicity of lead is an obstacle for their further applications. Within 2D HOIPs, the Pb(II) cation can be replaced by Sn(II), Ge(II), Cd(II), Mn(II), Fe(II), Cu(II) etc., while 2D HOIPs based on these metal cations are mainly investigated for the semiconducting property, photoluminescence, phase transitions and magnetism [36]. Recently, $(C_4H_9NH_3)_2(NH_3CH_3)_2Sn_3Br_{10}$ was discovered as a potential ferroelectric without evidence of polarization switching [37],
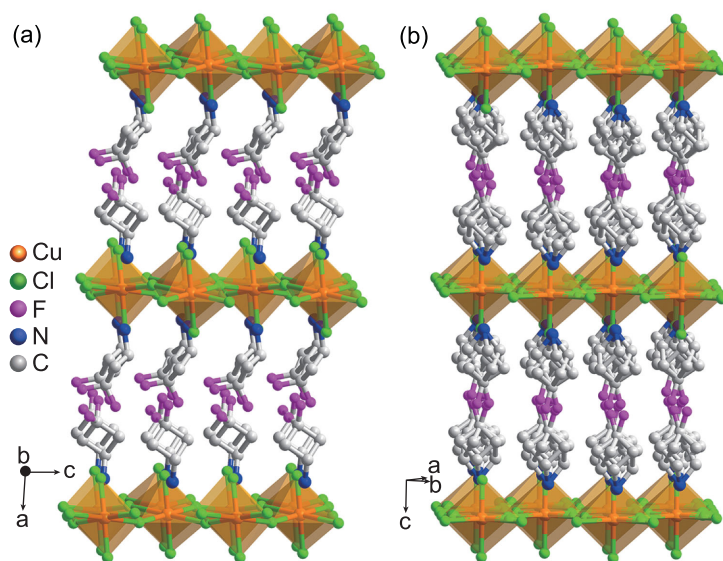
Figure 1. Packing views of the crystal structures of **1** at (a) 293 K and (b) 393 K.

and Ye *et al.* reported 2D organic-inorganic double perovskite ferroelectrics $[(R)$- and (S)-3-hydroxylquinuclidinium]$_4$KCe(NO$_3$)$_8$ [38]. Whereas, the lead-free 2D HOIP ferroelectrics remain very rare.

Regarding the application of ferroelectric materials, multiaxial ferroelectrics with multiple ferroelectric axes and equivalent polarization directions are highly preferable to uniaxial counterparts with one ferroelectric axis and two opposite polarization directions [39,40]. In the ferroelectric polycrystalline and thin-film sample, the more equivalent polarization directions allow easier and more effective polarization switching. Commercial ferroelectrics are generally multiaxial, and the multiaxial feature makes them widely used in the polycrystalline and thin-film form, as shown by the inorganic perovskite BaTiO$_3$ with three ferroelectric axes and six equivalent polarization directions [39,40]. In this respect, however, most of the 2D HOIP ferroelectrics are only uniaxial or biaxial [24–35], which also greatly restricts their future application; for example, the lead-free $[(R)$- and (S)-3-hydroxylquinuclidinium]$_4$KCe(NO$_3$)$_8$ are uniaxial ferroelectrics [38].

Here, we report a lead-free 2D Cu(II) halide HOIP multiaxial ferroelectric [3,3-difluorocyclobutylammonium]$_2$CuCl$_4$ ([DF-CBA]$_2$CuCl$_4$, **1**), which shows a 4/*mmm*F*m* ferroelectric phase transition at a high Curie temperature of 380 K, leading to four ferroelectric axes and eight equivalent polarization directions, larger than those of the other 2D HOIP ferroelectrics and the BaTiO$_3$. Interestingly, **1** also presents promi-

nent thermochromic behavior of color change from green-yellow to dark brown, which is not observed in lead halide 2D HOIP ferroelectrics. To our knowledge, **1** is the first multiaxial lead-free 2D HOIP ferroelectric. This pioneering work throws light on the exploration of new, excellent multiaxial lead-free 2D HOIP ferroelectrics with application prospects.

RESULTS AND DISCUSSION

We obtained single-crystals of **1** by slow evaporation of a methanol solution containing [3,3-difluorocyclobutylammonium]Cl and CuCl$_2$. Single-crystal X-ray diffraction experiments reveal that **1** crystallizes in the monoclinic polar *Cc* space group (point group *m* (C_{1h})) at 293 K in the ferroelectric phase (FP) (Supplementary Table S1). The crystal structure contains inorganic [CuCl$_4$]$^{2-}$ layers of corner-sharing CuCl$_6$ octahedral separated by organic [DF-CBA]$^+$ bilayers (Fig. 1a), showing the 2D organic-inorganic A$_2$BX$_4$ perovskite structure [36], where the [DF-CBA]$^+$, Cu^{2+} and Cl$^-$ ion corresponds to the A, B and X site, respectively. Thus, **1** can be regarded as the 2D halide perovskite, similar to the case of [CH$_3$NH$_3$]$_2$CuCl$_4$ [41]. The CuCl$_6$ octahedron is Jahn-Teller distorted with two Cu–Cl bond lengths (3.1635 and 3.0523 Å) obviously longer than the other four (2.2583–2.3179 Å) (Supplementary Table S2). The alternate elongated Cu–Cl bonds of the Jahn-Teller distorted CuCl$_6$ octahedra are perpendicular to each other, showing an anti-ferrodistortive arrangement in the *bc* plane (Supplementary Fig. S1), as found in [2,2′-(ethylenedioxy)bis(ethylammonium)]CuCl$_4$ [42]. The [DF-CBA]$^+$ cations are orientationally ordered, of which the C−N bonds align along one single orientation (Fig. 1a). The polar [DF-CBA]$^+$ cation with electric dipole moment shows an orientational arrangement along the *c* axis with all the C–N groups of [DF-CBA]$^+$ cations aligning along the *c* axis (Supplementary Fig. S2). Such an orientational arrangement of polar cations will induce a polarization [26]. Between the inorganic and organic components, there are weak N–H···Cl hydrogen-bonding interactions (Supplementary Fig. S3a), in which the average donor-acceptor distance is 3.350 Å.

At 393 K in the paraelectric phase (PP), the crystal symmetry of **1** changes to the tetragonal centrosymmetric P4$_2$/*mmc* space group (point group 4/*mmm* (D_{4h})). The relationship between the unit cell of FP and PP is $a^{FP} \approx c^{PP}$, $b^{FP} \approx \sqrt{2} a^{PP}$ and $c^{FP} \approx \sqrt{2} b^{PP}$. In the crystal structure, both the inorganic and organic constituents get seriously disordered (Fig. 1b). The atomic coordinates of the
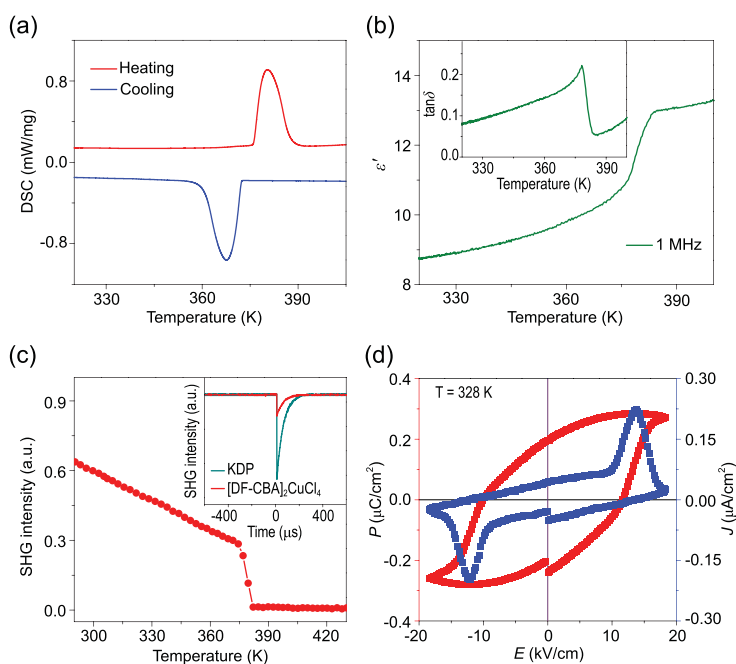
(a)

(b)

(c)

(d)

Figure 2. Ferroelectricity and related properties of **1**. (a) DSC curves. (b) Temperature-dependent ε' at 1 MHz upon heating. Inset: temperature-dependent $\tan\delta$ at 1 MHz upon heating. (c) Temperature-dependent SHG intensity upon heating. Inset: SHG signals of KDP and **1** at 293 K. (d) Ferroelectric hysteresis loop measured on the single-crystal sample along the *c* axis at 328 K by using the double-wave method.

four bridged Cl atoms of $CuCl_6$ octahedron were split into two positions (Fig. 1b and Supplementary Fig. S3b). The $[DF\text{-}CBA]^+$ cation exhibits a 4-fold orientational disorder with the C−N bonds having four orientations because it occupies the 2*mm* symmetry positions (Fig. 1b and Supplementary Fig. S3b). Thus, both the order-disorder transitions of the inorganic $[CuCl_4]^{2-}$ framework and the organic $[DF\text{-}CBA]^+$ cations contribute to the ferroelectric-to-paraelectric phase transition. In PP, the dipole moments of $[DF\text{-}CBA]^+$ cations cancel each other out because of the centrosymmetric crystal symmetry. We also confirm the structural phase transition of **1** by the variable-temperature powder X-ray diffraction (PXRD) experiments (Supplementary Fig. S4). The PXRD patterns at 293 K are consistent with the simulated ones from the crystal structure (Supplementary Fig. S4b) and show no obvious change with temperature increasing in FP. When the temperature increases to PP, the numbers of PXRD patterns reduce obviously, especially in the 2θ range from $16°$ to $24°$ (Supplementary Fig. S4a), which indicates a higher symmetry in PP. The experimental PXRD patterns at 393 K also match the simulated ones from the crystal structure (Supplementary Fig. S4c).

Differential scanning calorimetry (DSC) experiments reveal that the ferroelectric-to-paraelectric phase transition of **1** occurs at $T_c = 380$ K (T_c

is the phase transition temperature) (Fig. 2a). The phase transition is reversible and repeatable as reflected in the DSC curves recorded in three heating/cooling cycles (Supplementary Fig. S5). Thermogravimetric analysis (TGA) curves show that **1** is thermally stable up to 480 K (Supplementary Fig. S6), which is much higher than the phase transition temperature of 380 K. The dielectric anomaly near T_c in the temperature-dependent real part (ε'), loss ($\tan\delta$), and imaginary part ($\varepsilon'' = \varepsilon' \times \tan\delta$) of the complex permittivity of **1** at 1 MHz further verifies this phase transition (Fig. 2b and inset, and Supplementary Fig. S7). The ε' at 1 kHz, 10 kHz and 100 kHz shows obvious dielectric anomalies near 380 K as well (Supplementary Fig. S8). At lower frequencies, the dielectric anomalies are remarkable and become more like a peak shape (Supplementary Fig. S8). The peak temperature of the dielectric anomalies shows no obvious shift from the frequency of 1 kHz to 1 MHz, showing no dielectric relaxations. We also employed the temperature-dependent second harmonic generation (SHG) signal to study the phase transition. The SHG intensity of **1** has a certain value of about a quarter of that of KDP (potassium dihydrogen phosphate) at 293 K in the FP. It decreases to a zero value near T_c, and maintains zero values in the PP. This corresponds to the transition from the polar point group m (C_{1h}) to a centrosymmetric $4/mmm$ (D_{4h}) one. According to Aizu notion [43], the phase transition in **1** is the $4/mmmFm$ type ferroelectric. As Fig. 3a shows, from PP to FP, the symmetry breaks from 16 symmetry elements (E, $2C_4$, C_2, $2C'_2$, $2C''_2$, i, $2S_4$, σ_h, $2\sigma_v$ and $2\sigma_d$) in the $4/mmm$ (D_{4h}) point group to two (E and σ_h) in the m (C_{1h}) point group. Thus, **1** is a multiaxial ferroelectric with four ferroelectric axes and eight equivalent polarization directions. It is noted that the polarization directions of **1** are much more than those of other 2D HOIPs, most of which are uniaxial or biaxial ferroelectrics [24–35], and even more than the six polarization directions of typical inorganic perovskite ferroelectric $BaTiO_3$ (Fig. 3b) [39,40]. The multiaxial nature of **1** facilitates its applications in the thin-film form [39,40].

We then recorded the polarization-electric field (*P*–*E*) hysteresis loop of **1**. As shown in Fig. 2d, **1** presents a *P*–*E* hysteresis loop obtained on the single-crystal sample along the *c* axis at 328 K in the FP, directly proving the ferroelectricity. The saturate polarization (P_s) is estimated to be $0.29\ \mu C/cm^2$ from the loop, which is larger than that of the first molecular ferroelectric Rochelle Salt ($0.25\ \mu C/cm^2$) [44]. We also calculated the P_s of **1** based on the point charge mode (Supplementary Fig. S9). The experimental value is comparable to the calculated one ($0.328\ \mu C/cm^2$).

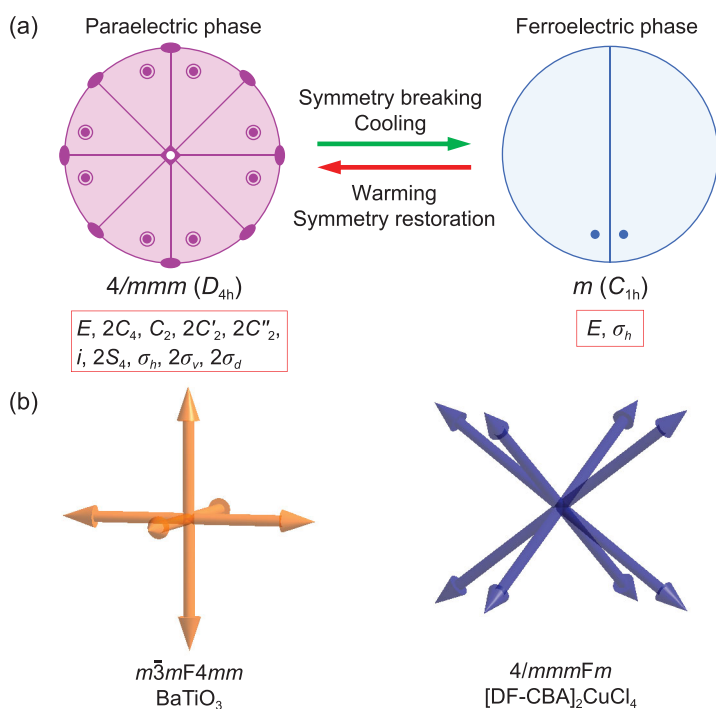**Figure 3.** (a) Symmetry change between the PP and FP in **1**. (b) Comparison of the polarization directions in BaTiO$_3$ and **1**.
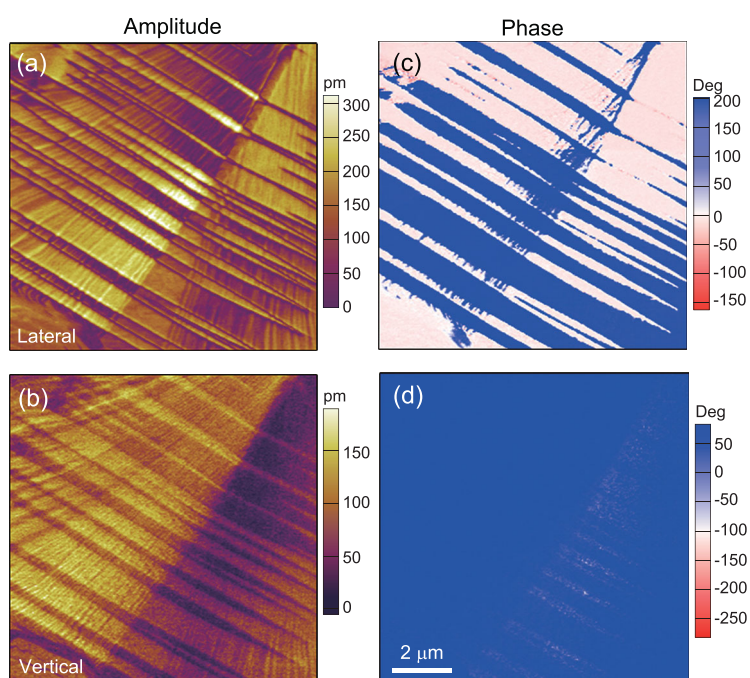

Figure 4. PFM imaging of domain pattern in the thin film of **1**. Lateral (a) and vertical (b) PFM amplitude images. Lateral (c) and vertical (d) PFM phase images.

We also characterized the domain structure of **1** on its thin film by piezoresponse force microscopy (PFM). The typical domain pattern was arranged in a stripe texture. An example is shown in Fig. 4. The stripe contrast can be clearly observed in both lateral and vertical amplitude images, in which the light and dark tones represent the local piezoresponse along the in-plane direction for lateral image and out-of-plane direction for vertical image. By comparison of the phase images, a uniform phase in the vertical phase image is seen. Contrastingly, in the lateral phase image the stripe domains were observed. The phase anisotropy of the vertical and lateral PFM modes indicates the existence of non-180° domain walls in the thin film, which thus reveals that **1** is a multiaxial ferroelectric.

Figure 5a and b respectively display the pristine vertical PFM amplitude and phase images of a region of 20 × 20 μm, together with the surface topography image shown in Fig. 5c. By locally poling the red-boxed region marked in Fig. 5e with positive voltage of +25 V, we found that a new domain was generated through the polarization switching. Next, a –20 V, 1 s duration voltage pulse was applied at the position '×' in the new domain. As a result, the partial of the new domain was switched back with 180° phase shift. Furthermore, local ferroelectric hysteresis loops can also be recorded by switching spectroscopy PFM measurements. A set of direct current (DC) voltage pulses up to ±20 V were applied to switching the polarization underneath the PFM tip, with a 5 V ac tip bias applied to record the corresponding piezoelectric amplitude and phase signal. As shown in Fig. 5f, 180° phase reversal occurs when a coercive voltage is exceeded. At the same time, hysteresis amplitude-bias butterfly loops were observed (Fig. 5i). Overall, our PFM measurements provide robust proof of the switchable polarization in **1**.

Interestingly, distinct from the 2D lead halide perovskite ferroelectrics, **1** exhibits thermochromic behaviors. Its crystal changes color obviously, reversibly and repeatedly from yellow-green at 293 K to a dark brown color at 393 K (Fig. 6a). The ultraviolet-visible (UV–Vis) absorption spectra at 293 K shows that **1** mainly absorbs light less than about 530 nm, matching with its yellow-green appearance. It is worth noting that there is a minor and broad absorption peak at around 750 nm in the absorption spectra, which is commonly found in 2D copper (II) chloride HOIP perovskites like [CH$_3$NH$_3$]$_2$CuCl$_4$ [41], and this absorption peak can be assigned to the d–d electronic transitions in the Cu^{2+} ions with the 3d^9 electronic configuration [41]. When the temperature increases, the main absorption band in the UV–Vis absorption spectra shows a remarkable red shift from 293 to 393 K (Fig. 6a). We also recorded the UV–Vis absorption spectra at different temperatures (Supplementary Fig. S10). The main absorption peaks at around 257 and 354 nm at 293 K show very slight red shifts when the temperature increases to 393 K. For the main absorption peak at around 435 nm at 293 K, it presents minor red shifts with temperature
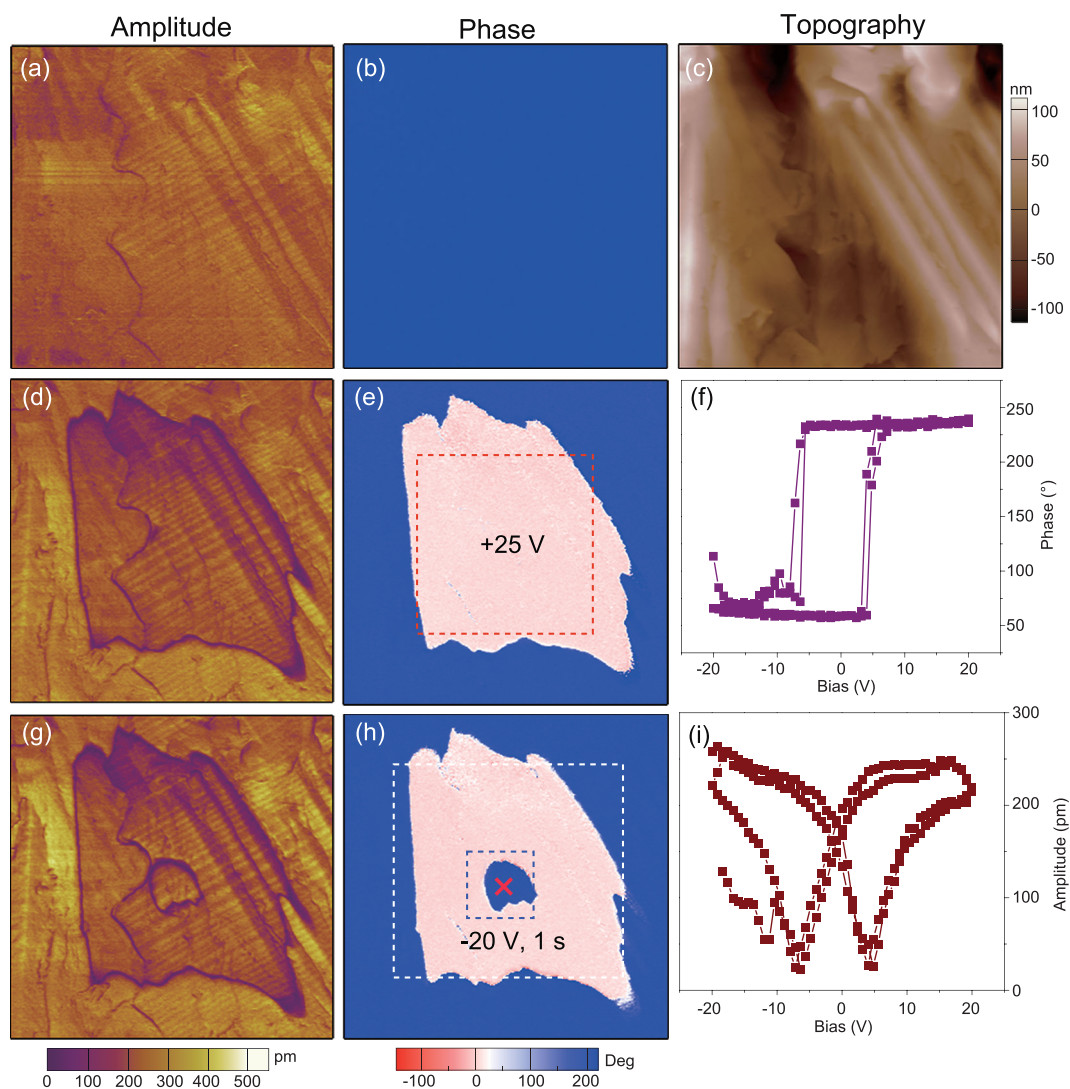
Amplitude	Phase	Topography

Figure 5. Polarization switching experiments for the thin film of **1**. (a) Initial PFM amplitude, (b) PFM phase and (c) topographic images of a region of 20 μm $\times$ 20 μm. (d) PFM amplitude and (e) phase images after applying voltage of +25 V on the red-boxed region. (g) PFM amplitude and (h) phase images after applying −20 V voltage pulse of 1 s duration on the point ×. PFM switching spectroscopy showing (f) square-like phase loops and (i) butterfly-like amplitude loops.

increasing below T_c of 380 K, and shows a relatively remarkable red shift from 373 K below the T_c to 393 K above T_c. When the temperature increases, the absorption edges of the main visible absorption band at around 524 nm at 293 K also show a remarkable red shift from 373 to 393 K. This indicates that the thermochromism of **1** is associated with the phase transition, as found in other thermochromic organic-inorganic Cu(II) halides showing phase transitions, in which the thermochromism is mainly related to the coordination environment change of copper (II) ion during the phase transition [45–47]. In **1**, the out-plane Cl–Cu–Cl bond angles of 86.43°–94.43° at 293 K in FP become 90.00° at 393 K in PP (Supplementary Fig. S11 and Table S2). The average long in-plane Cu–Cl bond distance

of 3.1515 Å, the average short in-plane Cu–Cl bond distance of 2.2590 Å and the average out-plane Cu–Cl bond distance of 2.2321 Å in PP are also obviously different from those in FP (3.1075 Å, 2.3155 Å and 2.2592 Å respectively). The changes of Cl–Cu–Cl bond angles and Cu–Cl bond distance show the geometry change of CuCl$_6$ octahedron, which contributes to the thermochromism.

In order to investigate the underlying cause of thermochromism, the HOMO (highest occupied molecular orbital) and LUMO (lowest unoccupied molecular orbital) of CuCl$_6$ octahedral configurations in FP and PP are calculated (Fig. 6b). The HOMO and LUMO in PP display distinct variation from those in FP. The resultant energy gap shifted from 0.1458 Ha (Hartree) in the FP to 0.1164 Ha of
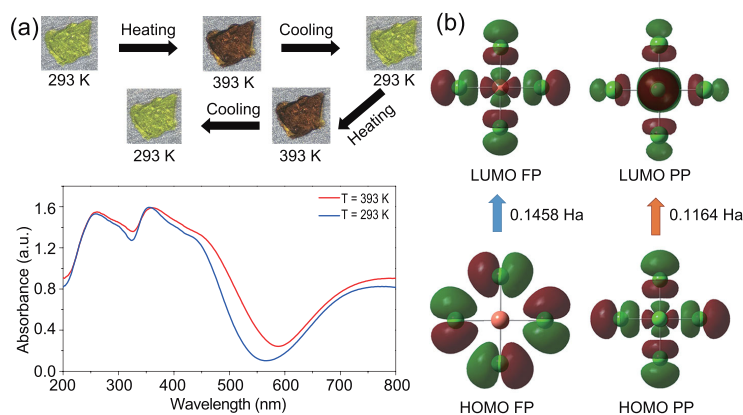
Figure 6. (a) Crystal (size: $1.1 \times 0.9 \times 0.5$ mm^3) color and solid-state UV–Vis absorption spectra of **1** at 293 and 393 K. (b) The HOMO and LUMO of CuCl$_6$ octahedral configurations in FP and PP of **1**.

PP. The large energy gap change could be attributed to the remarkable configuration change of CuCl$_6$ octahedral. Accordingly, the absorption edge will have a red shift tendency in the heating process from FP to PP, which is consistent with the experimental variable-temperature UV–vis absorption spectra.

CONCLUSION

In summary, we have presented a lead-free 2D HOIP ferroelectric, [3,3-difluorocyclobutyl-ammonium]$_2$CuCl$_4$, which undergoes a 4/*mmm*F*m* type ferroelectric phase transition at 380 K. Strikingly, **1** is a multiaxial ferroelectric with eight polarization directions, much more than those of 2D lead halide perovskite ferroelectrics, facilitating its application in the thin-film form. This is the first example of a 2D lead-free perovskite multiaxial ferroelectric. Moreover, during the ferroelectric-to-paraelectric phase transition, **1** shows remarkable thermochromism of color change from green-yellow to dark brown. This work opens up a pathway to constructing multiaxial lead-free 2D perovskite ferroelectrics.

METHODS
Sample preparation

The [3,3-difluorocyclobutylammonium]Cl ([DF-CBA]Cl) and CuCl$_2$ are commercially available. [DF-CBA]Cl (10 mmol) and CuCl$_2$ (5 mmol) were completely dissolved in methanol (100 ml). Slow evaporation of the solvent at room temperature obtains the crystals of [DF-CBA]$_2$CuCl$_4$ (yield, 98.5%). Single-crystal X-ray diffraction experiments reveal that the obtained crystals have the formula of [DF-CBA]$_2$CuCl$_4$ (Supplementary Table S1). The

phase purity of the as-grown crystals was confirmed by PXRD (Supplementary Fig. S4b). We prepared the thin film of [DF-CBA]$_2$CuCl$_4$ by spreading 10 μL precursor solution (100 mg as grow-crystals in 1 mL methanol) on ITO (indium tin oxide) coated glass substrate. Annealing the substrate at 313 K obtains the thin-film sample.

Characterization methods

Methods of XRD, DSC, dielectric, SHG, *P–E* loop, PFM and UV–vis absorption spectra measurements were described in detail previously [26,32]. The HOMO and LUMO are calculated at b3lyp/aug-cc-pVTZ level.

Accession codes

The structures have been deposited at the Cambridge Crystallographic Data Centre (deposition numbers: CCDC 1982768–1982769).

SUPPLEMENTARY DATA

Supplementary data are available at *NSR* online.

AUTHOR CONTRIBUTIONS

X.L. and R.-G.X. proposed and supervised the project. X.L. and R.-G.X. designed the research. C.-R.H. synthesized the sample. C.-R.H., X.-G.C., X.-J.S. and Z.-X.Z. carried out the characterizations. All authors analyzed the data, discussed the results and prepared the paper.

Conflict of interest statement. None declared.

REFERENCES

1. Tejuca LG and Fierro JL. *Properties and Applications of Perovskite-Type Oxides.* New York: CRC Press, 1993.
2. Li J, Zhong G and Xie S *et al.* Large-scale multiferroic complex oxide epitaxy with magnetically switched polarization enabled by solution processing. *Natl Sci Rev* 2020; **7**: 84–91.

3. Lu C, Wu M and Lin L *et al.* Single-phase multiferroics: new phenomena, and physics. *Natl Sci Rev* 2019; **6**: 653–68.

4. Li W, Wang Z and Deschler F *et al.* Chemically diverse and multifunctional hybrid organic-inorganic perovskites. *Nat Rev Mater* 2017; **2**: 16099.

5. Saparov B and Mitzi DB. Organic-inorganic perovskites: structural versatility for functional materials design. *Chem Rev* 2016; **116**: 4558–96.

6. Li JF, Li L and Zhang X *et al.* Practical high-performance lead-free piezoelectrics: structural flexibility beyond utilizing multiphase coexistence. *Natl Sci Rev* 2020; **7**: 355–65.

7. Li D, Shi J and Xu Y *et al.* Inorganic-organic halide perovskites for new photovoltaic technology. *Natl Sci Rev* 2018; **5**: 559–76.

8. Jena AK, Kulkarni A and Miyasaka T. Halide perovskite photovoltaics: background, status, and future prospects. *Chem Rev* 2019; **119**: 3036–103.

9. Stoumpos CC and Kanatzidis MG. Halide perovskites: poor man's high-performance semiconductors. *Adv Mater* 2016; **28**: 5778–93.

10. Manser JS, Christmas JA and Kamat PV. Intriguing optoelectronic properties of metal halide perovskites. *Chem Rev* 2016; **116**: 12956–3008.

11. Dou L, Wong AB and Yu Y *et al.* Atomically thin two-dimensional organic-inorganic hybrid perovskites. *Science* 2015; **349**: 1518–21.

12. Tsai H, Nie W and Blancon JC *et al.* High efficiency two-dimensional ruddlesden-popper perovskite solar cells. *Nature* 2016; **536**: 312–6.

13. Proppe AH, Quintero-Bermudez R and Tan H *et al.* Synthetic control over quantum well width distribution and carrier migration in low-dimensional perovskite photovoltaics. *J Am Chem Soc* 2018; **140**: 2890–6.

14. Mao L, Guo P and Kepenekian M *et al.* Structural diversity in white-light emitting hybrid lead bromide perovskites. *J Am Chem Soc* 2018; **140**: 13078–88.

15. Chen S and Shi G. Two-dimensional materials for halide perovskite-based optoelectronic devices. *Adv Mater* 2017; **29**: 1605448.

16. Zhong T, Li X and Wu M *et al.* Room-temperature multiferroicity and diversified magnetoelectric couplings in 2D materials. *Natl Sci Rev* 2020; **7**: 373–80.

17. Li LN, Sun ZH and Wang P *et al.* Tailored engineering of an unusual (C₄H₉NH₃)₂(CH₃NH₃)₂Pb₃Br₁₀ two-dimensional multilayered perovskite ferroelectric for a high performance photodetector. *Angew Chem Int Ed* 2017; **56**: 12150–4.

18. Wu ZY, Ji CM and Li LN *et al.* Alloying *n*-butylamine into CsPbBr₃ to give a two-dimensional bilayered perovskite ferroelectric material. *Angew Chem Int Ed* 2018; **57**: 8140–3.

19. Scott J. Applications of modern ferroelectrics. *Science* 2007; **315**: 954–9.

20. Zhu S. Novel ferroelectric tunnel junctions for nonvolatile memories. *Natl Sci Rev* 2014; **1**: 167–8.

21. Wang ZM and Gao S. Can molecular ferroelectrics challenge pure inorganic ones? *Natl Sci Rev* 2014; **1**: 25–6.

22. Zhu J, Huang F and Li Y *et al.* Dynamics and manipulation of ferroelectric domain walls in bismuth ferrite thin films. *Natl Sci Rev* 2020; **7**: 278–84.

23. Liu Y, Seidel J and Li J. Multiferroics under the tip: probing magnetoelectric coupling at the nanoscale. *Natl Sci Rev* 2019; **6**: 626–8.

24. Sha TT, Xiong YA and Pan Q *et al.* Fluorinated 2D lead iodide perovskite ferroelectrics. *Adv Mater* 2019; **31**: 1901843.

25. Ye HY, Liao WQ and Hu CL *et al.* Bandgap engineering of lead-halide perovskite-type ferroelectrics. *Adv Mater* 2016; **28**: 2579–86.

26. Liao WQ, Zhang Y and Hu CL *et al.* A lead-halide perovskite molecular ferroelectric semiconductor. *Nat Commun* 2015; **6**: 7338.

27. Li L, Liu X and Li Y *et al.* Two-dimensional hybrid perovskite-type ferroelectric for highly polarization-sensitive shortwave photodetection. *J Am Chem Soc* 2019; **141**: 2623–9.

28. Li LN, Shang XY and Wang SS *et al.* Bilayered hybrid perovskite ferroelectric with giant two-photon absorption. *J Am Chem Soc* 2018; **140**: 6806–9.

29. Zhang HY, Song XJ and Chen XG *et al.* Observation of vortex domains in a two-dimensional lead iodide perovskite ferroelectric. *J Am Chem Soc* 2020; **142**: 4925–31.

30. Wang S, Liu X and Li L *et al.* An unprecedented biaxial trilayered hybrid perovskite ferroelectric with directionally-tunable photovoltaic effects. *J Am Chem Soc* 2019; **141**: 7693–7.

31. Liu X, Wang S and Long P *et al.* Polarization-driven self-powered photodetection in a single-phase biaxial hybrid perovskite ferroelectric. *Angew Chem Int Ed* 2019; **58**: 14504–8.

32. Yang CK, Chen WN and Ding YT *et al.* The first 2D homochiral lead iodide perovskite ferroelectrics: [*R*- and *S*-1-(4-chlorophenyl)ethylammonium]₂PbI₄. *Adv Mater* 2019; **31**: 1808088.

33. Shi PP, Lu SQ and Song XJ *et al.* Two-dimensional organic-inorganic perovskite ferroelectric semiconductors with fluorinated aromatic spacers. *J Am Chem Soc* 2019; **141**: 18334–40.

34. Chen XG, Song XJ and Zhang ZX *et al.* Two-dimensional layered perovskite ferroelectric with giant piezoelectric voltage coefficient. *J Am Chem Soc* 2020; **142**: 1077–82.

35. Jia F, Hu S and Xu S *et al.* Persistent spin-texture and ferroelectric polarization in 2D hybrid perovskite benzylammonium lead-halide. *J Phys Chem Lett* 2020; **11**: 5177–83.

36. Mao L, Stoumpos CC and Kanatzidis MG. Two-dimensional hybrid halide perovskites: principles and promises. *J Am Chem Soc* 2019; **141**: 1171–90.

37. Li L, Liu X and He C *et al.* A potential Sn-based hybrid perovskite ferroelectric semiconductor. *J Am Chem Soc* 2020; **142**: 1159–63.

38. Shi C, Ye L and Gong ZX *et al.* Two-dimensional organic-inorganic hybrid rare-earth double perovskite ferroelectrics. *J Am Chem Soc* 2019; **142**: 545–51.

39. Tang YY, Li PF and Liao WQ *et al.* Multiaxial molecular ferroelectric thin films bring light to practical applications. *J Am Chem Soc* 2018; **140**: 8051–9.

40. Ye HY, Ge JZ and Tang YY *et al.* Molecular ferroelectric with most equivalent polarization directions induced by the plastic phase transition. *J Am Chem Soc* 2016; **138**: 13175–8.

41. Cortecchia D, Dewi HA and Yin J *et al.* Lead-free MA₂CuClₓBr₄₋ₓ hybrid perovskites. *Inorg Chem* 2016; **55**: 1044–52.

42. Jaffe A, Lin Y and Mao W L *et al.* Pressure-induced conductivity and yellow-to-black piezochromism in a layered Cu–Cl hybrid perovskite. *J Am Chem Soc* 2015; **137**: 1673–8.

43. Aizu K. Possible species of 'ferroelastic' crystals and of simultaneously ferroelectric and ferroelastic crystals. *J Phys Soc Jpn* 1969; **27**: 387–96.

44. Zhang W and Xiong RG. Ferroelectric metal-organic frameworks. *Chem Rev* 2012; **112**: 1163–95.

45. Willett RD, Haugen JA and Lebsack J *et al.* Thermochromism in copper(II) chlorides: coordination geometry changes in CuCl₄²⁻ anions. *Inorg Chem* 1974; **13**: 2510–3.

46. Sun B, Liu XF and Li XY *et al.* Reversible thermochromism and strong ferromagnetism in two-dimensional hybrid perovskites. *Angew Chem Int Ed* 2020; **59**: 203–8.

47. Liu JC, Liao WQ and Li PF *et al.* A molecular thermochromic ferroelectric. *Angew Chem Int Ed* 2019; **59**: 3495–9.